Solid-State Electronics 201 (2023) 108590

Contents lists available at ScienceDirect

Solid State Electronics

journal homepage: www.elsevier.com/locate/sse

The influence of interface effects on the switching behavior in ultra-scaled MRAM cells☆

M. Bendra [a,b,*], S. Fiorentini [a,b], W. Goes [c], S. Selberherr [b], V. Sverdlov [a,b]

[a] Christian Doppler Laboratory for Nonvolatile Magnetoresistive Memory and Logic at the Institute for Microelectronics, TU Wien, Gußhausstraße 27-29, A-1040 Wien, Austria
[b] Institute for Microelectronics, TU Wien, Gußhausstraße 27-29, A-1040 Wien, Austria
[c] Silvaco Europe Ltd., Cambridge, United Kingdom

ARTICLE INFO

Keywords:
Spin-transfer torques
Ultra-scaled MRAM
Interfacial-perpendicular magnetic anisotropy

ABSTRACT

The development of advanced magnetic tunnel junctions with a single-digit nanometer footprint can be achieved using an elongated multilayered ferromagnetic free layer structure. In this work, we demonstrate the switching of a composite free layer consisting of two ferromagnets separated by an MgO layer and an additional capping MgO layer to boost perpendicular anisotropy. This serially connected MTJs form a multi-state memory cell. Because of the ability to store data in more than one bit (0 or 1), the memory density can be increased, making the memory more efficient and cost-effective. A proper design of the free layer and its interface-induced perpendicular anisotropy helps to achieve reliable switching.

1. Introduction

Emerging nonvolatile spin-transfer torque (STT) magnetoresistive random access memory (MRAM) is one of the most promising candidates for future memory due to excellent performance and CMOS compatibility for embedded applications [1]. STT-MRAM has been increasingly adopted as a reliable, persistent nonvolatile memory capable of supporting the growing computing memory demands from data centers to wearables, artificial intelligence [2], and IoT [3]. To replace the ubiquitous DRAM, scaling STT-MRAM down to achieve higher densities is a key task, as well as improving the endurance and write speed [4]. STT-MRAM shows promise as universal memory, with the attributes of SRAM, DRAM, and small to medium capacity storage memory [5]. Devices based on perpendicular magnetic anisotropy (PMA) have attracted much attention because of the scaling advantages due to a strong PMA, good tunnel magnetoresistance ratio, and low critical switching current density [6]. Studies have shown that PMA originates from the interface between CoFeB and MgO [7]. The tunnel magnetoresistance (TMR) and resistance area product mainly depends on the MgO tunneling layer quality [8,9]. In recent years, double free layer structures, such as MgO|CoFeB|MgO|CoFeB stacks, have received widespread attention because of the enhanced PMA arising from multiple MgO|CoFeB interfaces providing high thermal stability [10].

In particular, the design of advanced single-digit nanometer footprint MRAM cells requires precise knowledge of spin currents and torques in magnetic tunnel junctions (MTJs) with elongated free and reference layers. Interface induced effects, like the perpendicular anisotropy and the spin-transfer torque, must be carefully evaluated. For this purpose, we have carefully modeled the interface effects through the use of position-dependent parameters and applied them to a device with several tunnel barrier interfaces with a few nanometers, diameter. The predicted switching behavior of ultra-scaled MRAM cells with several MgO interfaces agrees well with recent experimental results [11].

A conventional MRAM cell consists of several layers, including a CoFeB reference layer (RL) and a free magnetic layer (FL) separated by an MgO tunnel barrier (TB) or by an nonmagnetic spacer (NMS), cf. Fig. 1(b) and (c). The magnetization configuration perpendicular to the TB is determined by the anisotropy induced by the interface at the CoFeB|MgO interface. To further increase the perpendicular magnetic anisotropy, additional CoFeB|MgO interfaces are added in the FL, cf. Fig. 1(a) [12]. To reduce the cell diameter and to further boost the perpendicular anisotropy, one elongates the FL along the direction normal to the CoFeB|MgO interfaces [11]. With the length of the FL increasing to the order of or even larger than the diameter of the FL, the shape anisotropy becomes an important contribution to the perpendicular anisotropy. However, the interface-induced anisotropy still plays a decisive role in defining the switching of elongated composite FLs made

☆ The review of this paper was arranged by Pierpaolo Palestri.

* Corresponding author.
E-mail address: bendra@iue.tuwien.ac.at (M. Bendra).

https://doi.org/10.1016/j.sse.2023.108590

Available online 9 January 2023

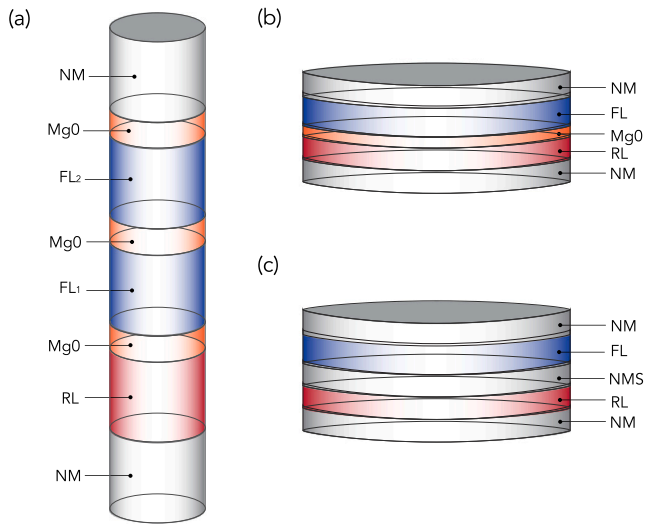

Fig. 1. (a) Ultra-scaled MRAM cell with a diameter of 2.3 nm, a 5 nm RL, a 0.9 nm TB, and a composite FL, consisting of two ferromagnetic parts separated by a 0.9 nm MgO layer. The FL is capped by an additional MGO layer of 0.9 nm thickness. (b) Conventional MRAM cell with a diameter of 40 nm, a 1 nm RL, a 1.7 nm FL, and a 1 nm TB or (c) an NMS which consists of a 2 nm metal film.

of several pieces separated by MgO barriers as will be demonstrated below.

2. Method

2.1. Modeling interface effects

To investigate the influence of the interface effects on the switching behavior, we model the interface-induced anisotropy as (*i*) an average constant contribution to the uniaxial bulk anisotropy (shown inFig. 2(a) with the red-dashed line) and as (*ii*) localized near the interface (blue solid line inFig. 2(a)). We employ a cubic function describing the transition between the interface and the bulk value. We set the derivative to zero at the transition points in order to have a smooth change. Furthermore, we investigate different lengths of the transition region τ, where the interface-induced anisotropy is localized. In particular, we examine four different lengths of the transition region, the related dependence of the anisotropy coefficient is depicted in Fig. 2(a). The blue solid line shows the case of a 1 nm transition region, while the cyan, violet, and green dot-dashed lines represent the cases of a length of 0.5 nm, 1.5 nm, and 2.5 nm, respectively. A higher length implies a slower decay of the anisotropy inside the magnetic layers. The strength of the interface anisotropy $\mathbf{K_i}$ employed for the simulations is $1.53 \cdot 10^{-3}\ \frac{\mathrm{mJ}}{\mathrm{m}^2}$, consistent with experimental values [7,11]. In the absence of bulk crystalline anisotropy, the value of the constant uniaxial anisotropy coefficient $\mathbf{K}$ resulting from each interface is given by $\mathbf{K_i}/\mathbf{t_{CoFeB}}$, where $\mathbf{t_{CoFeB}}$ is the length of the CoFeB layer. For the localized anisotropy coefficients depicted inFig. 2(a), the decay functions where chosen so that they have the same integral over the transition region τ with a value equal to $\mathbf{K_i}$.

We also consider different behaviors for the transverse spin dephasing length shown in Fig. 2(b). The value of the spin dephasing length determines the characteristic distance over which the non-equilibrium spin accumulation due to the electric current running through the structure decays from its maximum value at the FL interface to zero inside the FL. Therefore, the spin dephasing length defines the size of the layer close to the FL interface where the STT is acting. A short effective value of the dephasing length of $\lambda_\varphi = 0.4$ nm ensures rapid absorption of the transverse spin components, in agreement with circuit theory [13], and localizes the torque near the interfaces [14], as expected in strong ferromagnets [15,16].

Table 1
Simulation parameters.

Parameter	Value
Gilbert damping, α	0.02
Gyromagnetic ratio, γ	$1.76 \cdot 10^{11}\ \frac{\mathrm{rad}}{\mathrm{s\ T}}$
Saturation magnetization, M_S	$1.2 \cdot 10^{6}\ \frac{\mathrm{A}}{\mathrm{m}}$
Exchange constant, A	$1 \cdot 10^{-11}\ \frac{\mathrm{J}}{\mathrm{m}}$
Uniaxial anisotropy constant, K	$0.6 \cdot 10^{6}\ \frac{\mathrm{J}}{\mathrm{m}^3}$
Current spin polarization, β_σ	0.7
Diffusion spin polarization, β_D	1.0
Electron diffusion coefficient, D_e	$2 \cdot 10^{-2}\ \frac{\mathrm{m}^2}{\mathrm{s}}$
Spin-flip length, λ_{sf}	10 nm
Exchange length, λ_J	1 nm
Electrical resistance in the anti-parallel state, R_{AP}	750 kΩ
Electrical resistance in the parallel state, R_P	410 kΩ

However, the bulk value of the spin dephasing length can be larger than the employed effective short value near the interface (blue line in Fig. 2(b)), allowing the torques to act on larger portions of the FL. For this purpose, we employ the same transition regions described before in order to let the spin dephasing length go from its low value close to the interface to a higher bulk value of 5 nm. The functions describing this transition are depicted in Fig. 2(b), where the solid blue line represents the behavior for a transition region of 1 nm, and the cyan, violet, and green dot-dashed lines represent the behavior for transition regions of 0.5 nm, 1.5 nm, and 2.5 nm, respectively. A higher τ value implies a slower transition of λ_φ from its effective interface value to the bulk value.

2.2. Micromagnetic modeling

To model the dynamic properties of an ultra-scaled MRAM cell, we employ a fully three-dimensional finite element method solver based on the Open Source library MFEM [17], including all physical phenomena, described with Eqs. (1)–(6). The magnetization dynamics are captured by the Landau–Lifshitz–Gilbert equation (LLG).

$$\frac{\partial \mathbf{m}}{\partial t} = -\gamma \mathbf{m} \times \mathbf{H}_{\mathrm{eff}} + \alpha \mathbf{m} \times \frac{\partial \mathbf{m}}{\partial t} + \frac{1}{M_S}\mathbf{T_S} \tag{1}$$

$\mathbf{m} = \mathbf{M}/M_S$ is the position-dependent normalized magnetization, M_S is the saturation magnetization, α is the Gilbert damping constant, γ is the gyromagnetic ratio, and μ_0 is the vacuum permeability. The effective field $\mathbf{H}_{\mathrm{eff}}$ includes the magnetic anisotropy field, the exchange field, and the demagnetization field. The latter contribution to $\mathbf{H}_{\mathrm{eff}}$ is evaluated only on the disconnected magnetic domains with a hybrid approach combining the boundary element method and the finite element method [18]. The magnitude of the anisotropy field contribution $\mathbf{H}_{\mathrm{K}}$ is related to the coefficient $\mathbf{K}$ described before as $\mathbf{H}_{\mathrm{K}} = 2 \cdot \mathbf{K}/(\mu_0 \cdot M_S)$. To appropriately model the switching of ultra-scaled MRAM cells, a complete description of the torque term $\mathbf{T_S}$ is used to include all physical phenomena responsible for proper operation of the MRAM cell.

$$\mathbf{T_S} = -\frac{D_e}{\lambda_J^2}\mathbf{m} \times \mathbf{S} - \frac{D_e}{\lambda_\varphi^2}\mathbf{m} \times (\mathbf{m} \times \mathbf{S}) \tag{2}$$

The torque is generated by a non-equilibrium spin accumulation $\mathbf{S}$ acting on the magnetization via the exchange interaction. λ_J is the exchange length, λ_φ is the spin dephasing length, and D_e is the electron diffusion coefficient in the ferromagnetic layers. The drift-diffusion formalism has already been successfully applied in a spin-valve structure with a non-magnetic spacer layer [19–21]. The coupled spin and charge drift-diffusion model, as defined by Eqs. (3)–(5) supplemented by the

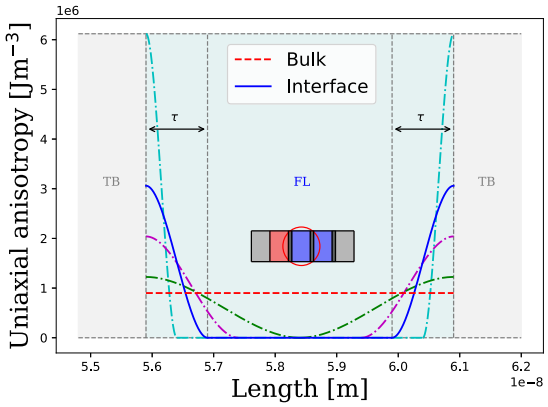

(a) The position-dependent development of interface anisotropy (blue), in comparison to a constant averaged anisotropy value applied within the 1st part of the FL (red). The dot-dashed curves represent different transition regions τ for the interface anisotropy.

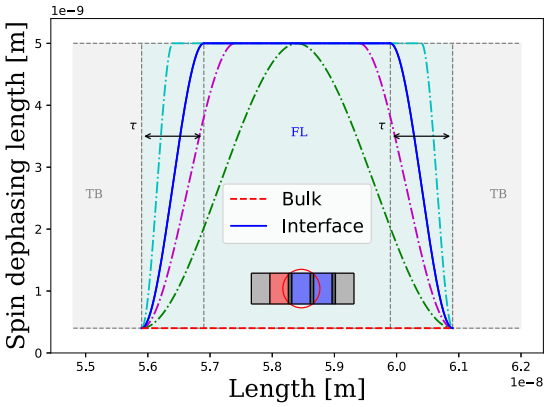

(b) The transverse spin dephasing length. The blue line represents the position-dependent development and the dashed red line the bulk/constant value, along the structure.

Fig. 2. Interface-induced perpendicular anisotropy and the transverse spin dephasing length.

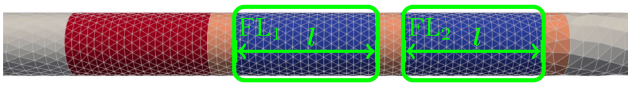

Fig. 3. Simplified mesh of the first simulated structure. This composite structure consists of a CoFeB (5)|MgO (0.9)|CoFeB (5)|MgO (0.9)|CoFeB (5)|MgO (0.9) MTJ connected to normal metal contacts (50), where the numbers in parentheses indicate the thickness of each layer in nanometer. The diameter is 2.3 nm. A bias of 2 V is applied across the structure. The colors correspond to those in the graphic, cf. Fig. 1(a). The green framed section denotes the FL segments for FL_1 and FL_2, with the length l.

appropriate boundary conditions, accurately describes the charge and the spin transport through a nanometer sized magnetic valve [22].

$$D_e\left(\frac{\mathbf{S}}{\lambda_{sf}^2}+\frac{\mathbf{S}\times\mathbf{m}}{\lambda_J^2}+\frac{\mathbf{m}\times(\mathbf{S}\times\mathbf{m})}{\lambda_\varphi^2}\right)=-\nabla\cdot\mathbf{J_S} \tag{3}$$

$$\mathbf{J_S}=-\frac{\mu_B}{e}\beta_\sigma\left(\mathbf{J_C}\otimes\mathbf{m}+\beta_D D_e\frac{e}{\mu_B}[(\nabla\mathbf{S})\mathbf{m}]\otimes\mathbf{m}\right)-D_e\nabla\mathbf{S} \tag{4}$$

$$\mathbf{J_C}=\sigma\mathbf{E}-\beta_D D_e\frac{e}{\mu_B}[(\nabla\mathbf{S})\mathbf{m}] \tag{5}$$

μ_B is the Bohr magneton, e is the electron charge, and β_σ and β_D are polarization parameters. $\otimes$ is the outer product, $\mathbf{J_C}$ is the charge current density, and $\mathbf{J_S}$ is the spin current. We extended this method to MTJs by modeling the TB as a poor conductor with a local resistance (6) dependent on the relative orientation of the FL magnetization [23].

$$\sigma(\theta)=\frac{\sigma_P+\sigma_{AP}}{2}\left(1+\left(\frac{\mathrm{TMR}}{2+\mathrm{TMR}}\right)\cos\theta\right) \tag{6}$$

σ_P (σ_{AP}) is the conductivity in the P (AP) state, and θ is the local angle between the magnetic vectors in the free and reference layer. The tunneling magnetoresistance is defined as

$$\mathrm{TMR}=\frac{\mathrm{G}_P-\mathrm{G}_{AP}}{\mathrm{G}_{AP}} \tag{7}$$

G_P (G_{AP}) is the conductance in the P (AP) state. A high TMR is important to be able to read the conductance difference between the two configurations. When the electrons cross the RL, they become spin-polarized, generating a spin current. They then enter the FL, where the spin current acts on the magnetization. If the current is sufficiently strong, the magnetization of the free layer can be switched between the two stable configurations, parallel or anti-parallel, relative to the RL.

2.3. Simulated structures

For our simulations, five different structures were considered. In Fig. 3 a simplified mesh of a cylindrical composite STT-MRAM structure is shown. The MTJ stack consists of CoFeB (5)|MgO (0.9)|CoFeB (5)|MgO (0.9)|CoFeB (5)|MgO (0.9) connected to normal metal contacts (50), where the numbers in parentheses indicate the length of each layer in nanometers. To further investigate the effect of the interface values, we varied the length l of both free layer parts (cf. Fig. 3 green framed sections) with the following values: 2 nm, 3 nm, 4 nm, and 7.5 nm. The relevant parameters are listed in Table 1.

3. Results

We analyze the effects of the models introduced in Section 2.1 for the uniaxial magnetic anisotropy constant (Fig. 2(a)) and the spin dephasing length (Fig. 2(b)) on the switching behavior. In order to integrate the LLG Eq. (1) numerically, a backward-Euler scheme with a constant time step of 0.1 ps was used. We have checked that a two times finer stepping does reproduce the same switching behavior for all models considered. This step is crucial for the simulation of the domain wall motion, because the transition of the magnetization between the domains must be resolved. Failure to do so may result in artificial locking of the domain wall on the computational grid.

In order to simulate the switching, we apply a constant voltage of two volts to the structure shown in Fig. 3, with a length of the FL's of 5 nm. We fix the localization length τ at 1 nm for concreteness. We compare the switching behavior for a combination of the cases when the perpendicular anisotropy is a constant throughput the free layer (bulk) of if it is localized close to the interfaces within τ (interface). Additionally, we consider also the case of constant spin dephasing length bulk and the interface case when the dephasing is stronger within τ close to the interfaces as shown in Fig. 2(a) (blue line).

Fig. 4(a) shows the time evolution of the out-of-plane magnetization component when switching from the anti-parallel (AP) to parallel (P) configuration of the free and fixed layers, for different combination of the bulk and interface cases. The magnetization reversal is similar regardless of the model used. The AP to P switching with the interface model for magnetic anisotropy (interface-induced anisotropy) is about 10% slower. Fig. 4(b) shows, however, that switching from P to AP with the bias of 2 V is accelerated, when the perpendicular magnetic anisotropy is interface-induced. The choice of an interface model for

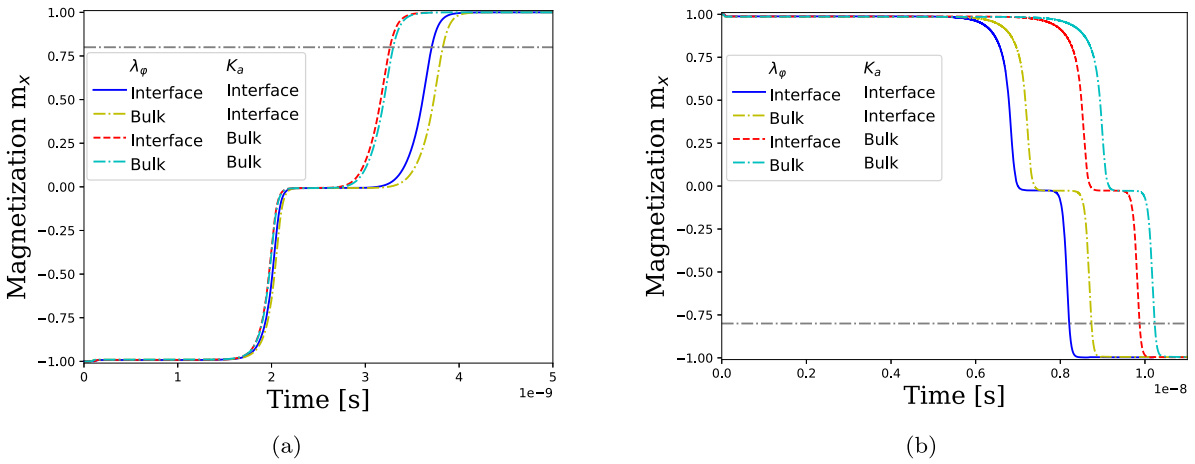

Fig. 4. Magnetization trajectories for switching from (a) AP to P and (b) P to AP, for various combinations of bulk and interface anisotropy and spin dephasing length. The transition region τ is 1 nm for both **K** and λ_φ, and the length of the FL's is 5 nm. The horizontal gray dot-dashed line correspond to 80% switched.

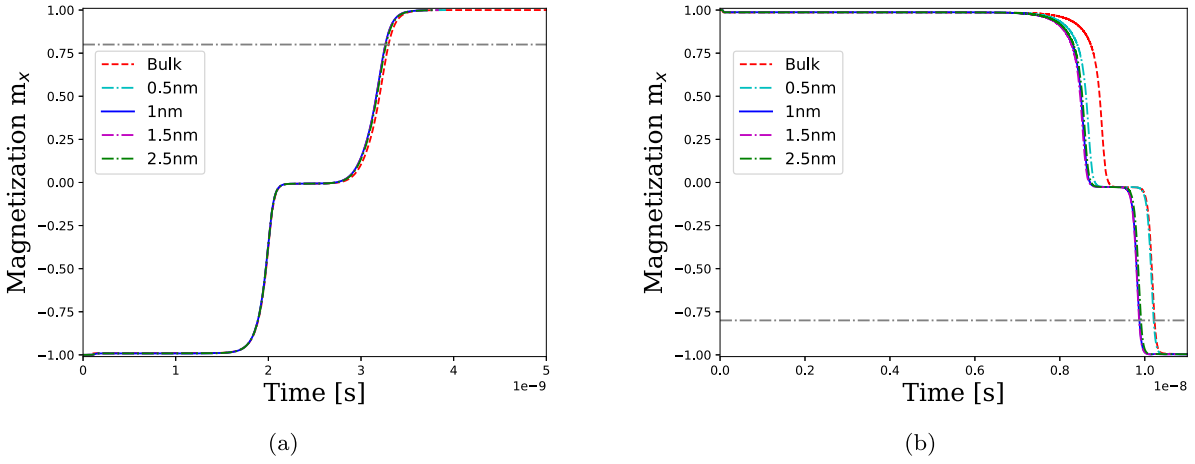

Fig. 5. Magnetization trajectories for switching from (a) AP to P and (b) P to AP, for various localization lengths τ for the spin dephasing length, and for the FL's length of 5 nm. The horizontal gray dot-dashed line correspond to 80% switched.

spin dephasing length over a bulk one has less impact on the switching behavior.

To investigate this behavior further, we now consider the length of the transition region τ to be 0.5 nm, 1 nm, 1.5 nm, and 2.5 nm, for the spin dephasing interface model. The value of τ determines the length scale over which λ_φ rises from its interface value of 0.4 nm to the bulk value of 5 nm. The bias is −2 V or 2 V depending on the configuration, AP to P or P to AP, is applied. In order to determine the influence of the transition region length for the spin dephasing length on the switching process, the anisotropy coefficient is taken as average bulk value.

Fig. 5 reports switching results obtained with the different transition region lengths for the spin dephasing. Fig. 5(a) shows that an almost identical behavior is obtained for AP to P switching, and for the P to AP switching, independent of the length of the transition region. The negligible role in the choice of the length of the transition region for the spin dephasing length is due to the fact that even at a constant bulk value of the spin dephasing, the torque acts already very close to the interface, as shown in Fig. 6, and an additional torque confinement due to a stronger dephasing at the interface does not result in switching modulations.

Now we consider the role of localization at the interfaces of the perpendicular magnetic anisotropy. Several values of τ are considered. We fix the spin dephasing length at its bulk value of 0.4 nm. A longer τ implies a slower decay of the anisotropy coefficient and its less prominent localization near the interface. Fig. 7 displays the switching behavior for several lengths of the transition region for uniaxial

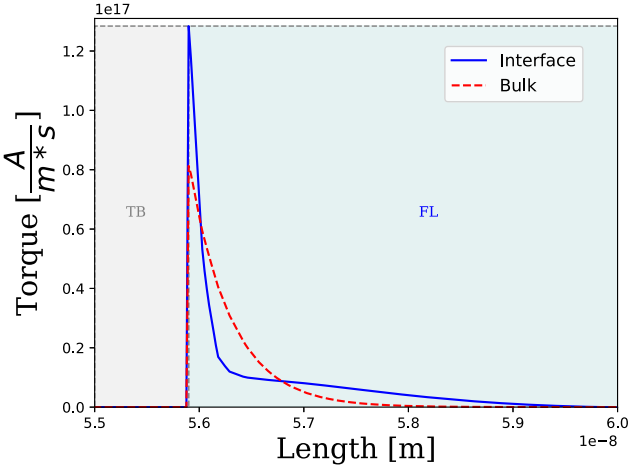

Fig. 6. Damping-like torques computed in a structure with semi-infinite ferromagnetic leads with a bias of −2 V and magnetization along x in the RL and along z in the FL, for constant dephasing length in blue, and comparison to the position dependent dephasing length in red.

anisotropy. For AP to P switching, the interface-induced anisotropy

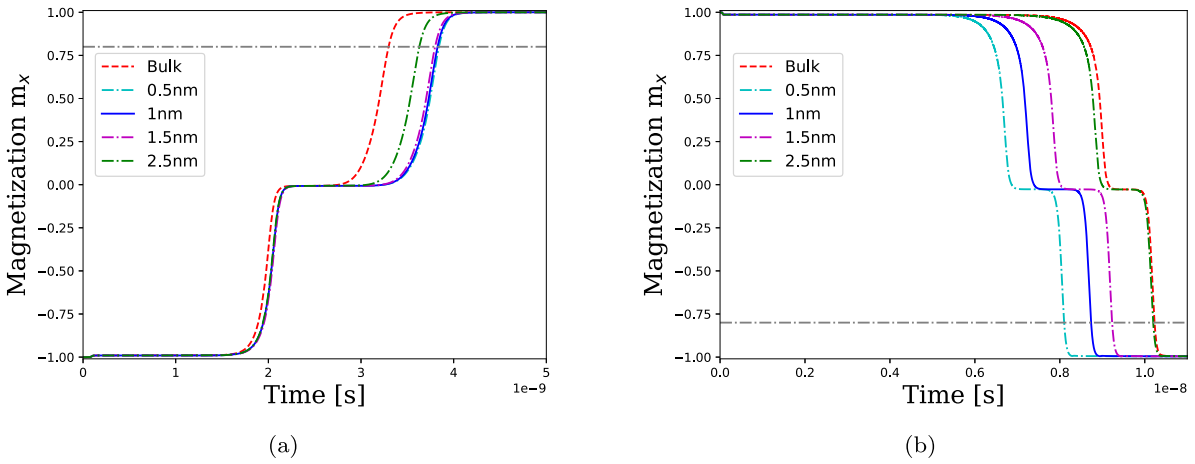

Fig. 7. Magnetization trajectories for switching from (a) AP to P and (b) P to AP, for various transition regions τ for localized anisotropy, and for the FL's length of 5 nm. The horizontal gray dot-dashed line correspond to 80% switched.

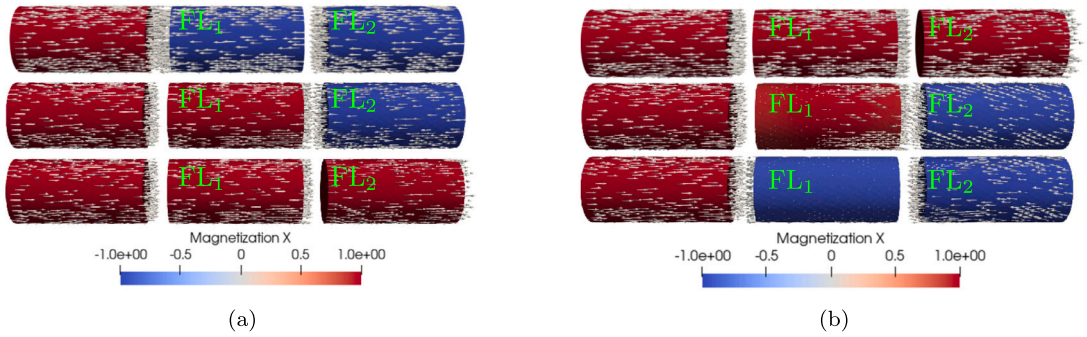

Fig. 8. Switching snapshot of MRAM cell's in the following order: Initial, intermediate and final state, for the configuration (a) AP to P and (b) P to AP. Arrows indicate the magnetization directions, and color-coding represents the average magnetization in x-direction.

moderately slows the switching down. This is due to a sturdier perpendicular orientation of the magnetization being enforced near the interface, where the torque is acting, resulting in a slower switching of the FL2 compared to the uniformly distributed magnetic anisotropy. For P to AP switching both ends of the layer start precessing around the demagnetization field, but with different amplitudes and frequencies. These oscillations propagate all the way through the FL, until the middle bulk part is flipped. If the magnetic anisotropic is uniformity distributed, it becomes more difficult to flip the FL compared to the case with the anisotropy localized at the interfaces and not in the bulk. The relative difference in switching times reaches 10 – 15% demonstrating the importance of accurately modeling the interface-induced anisotropy effects on switching of elongated magnetic layers.

We note that both Figs. 4 and 5 display a distinct peculiarity at both AP to P and P to AP switching. Namely, the magnetization of the FL develops a plateau around $m_x = 0$. The plateau is due to the fact that the magnetization of the two similar parts composing the FL are anti-parallel to each other. It then follows that the magnetization reversal is a sequential process in which one part of the FL switches first followed by the magnetization reversal of the remaining part. Fig. 8(a) demonstrates the switching sequence for the AP to P process. We note that the sequential switching of the composite FL is not universal: Although the two elongated part switch sequentially for the parameters chosen in Table 1, a more coherent switching of both parts of the composite FL was predicted by [24] and can be achieved with a different set of parameters. In the AP configuration, both the RL and the right part of the FL (FL_2 cf. Fig. 3) exert a torque on the first, left, section of the FL (FL_1 cf. Fig. 3) in the same direction, making it switch first. As the torques from the RL and FL_2 are additive and act in the same direction, the switching of FL_1 is fast, cf. Fig. 4(a). At the same time, the torque from FL_1 towards FL_2 is acting to keep the two sections parallel to each other, and therefore preserves the orientation. However, after the magnetization of FL_1 is inverted and becomes parallel to that of the RL, the torque from FL_1 acting on FL_2 changes its sign forcing FL_2 to switch. As the torque acts only from FL_1, the magnitude of the torque acting on FL_2 is smaller than that previously acting on FL_1. The weaker torque results in a slower switching of FL_2, cf. Fig. 4(a).

When going from P to AP, the opposite process happens. Snapshots of the important stages of the switching process for the P to AP configuration are shown in Fig. 8(b). The torque acting from FL_2 on FL_1 is opposite to that from the RL, so that FL_2 switches first. As only the torque from FL_1 is acting on FL_2, the switching time of FL_2 is relatively slow. After FL_2 has switched, the torque contributions from FL_2 and the RL act on FL_1 in the same direction, completing the switching fast. As the parts of the FL are elongated, the exchange interaction is not sufficient to ensure a uniform macrospin-like switching of the FL_1 and FL_2 parts. The torques are the strongest close to the interface, so it is beneficiary to have the uniaxial anisotropy localized close to the interface, where it can be easier overcome by the torques, to accelerate the switching at least for the P to AP switching. The overall switching behavior agrees well with reported experimental results [11].

To evaluate the performance of the proposed elongated MRAM cells, we vary the length of the FL. Fig. 9 shows the AP to P and P to AP switching results for different combinations of a bulk, and an interface model for magnetic anisotropy and spin dephasing length. Again, a bias of 2 V is applied. A transition region of 0.5 nm for the interface cases of the magnetic anisotropy and of 1 nm for the interface spin dephasing model are considered.

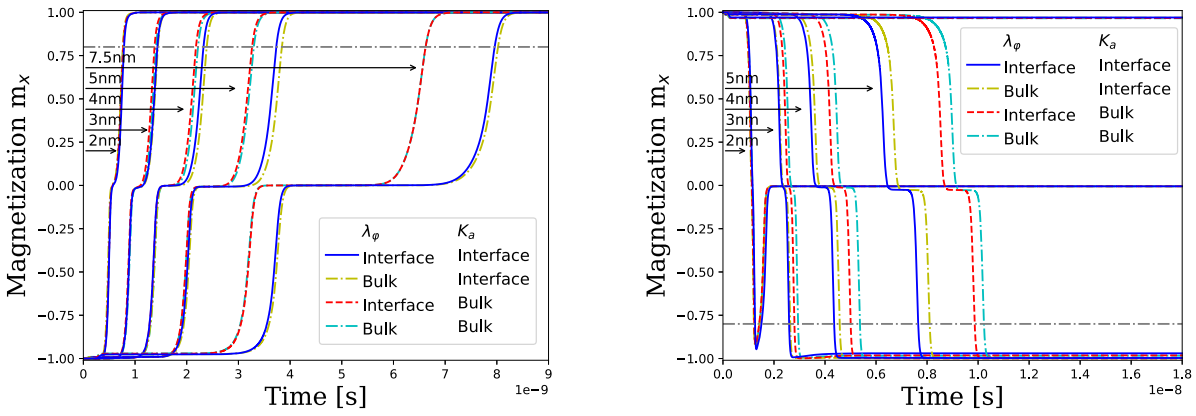

(a) (b)

Fig. 9. Magnetization trajectories for switching from (a) AP to P and (b) P to AP, for various structures for localized spin dephasing length. The horizontal gray dot-dashed line correspond to 80% switched.

We observe that at the beginning of switching the plateau around $m_x = 0$ is hardly present at a length of the FL of 2 nm. Furthermore, the difference between the bulk and interface models of **K** and λ_φ is not visible for short FLs, when the FL length is about the length of a transition region. As the length of the FL increases, the time duration of the plateau also increases. The difference between the bulk and interface models of **K** and λ_φ increases. We note that all structures switched successfully in Fig. 9(a). However, Fig. 9(b) demonstrates that the applied voltage of 2 V is not sufficient to achieve switching of the structure with 7.5 nm long FL's. It is due to the fact the stray fields which become strong for 7.5 nm FL's parts prevent the FL_1 and FL_2 to switch in an AP configuration, and a larger voltage must be applied.

Moreover, the structure with 2 nm short FLs gets close to complete switching, before getting locked at the middle $m_x = 0$ value of the magnetization. This is because, after the FL reaches the parallel configuration shown in Fig. 8(b), the torque from FL_1 to acting on FL_2 is strong enough to overcome the stray fields and to bring FL_1 and FL_2 into an AP configuration. These results imply that, for ultra-scaled MRAM cells, the length of the layers must to be sufficiently large to avoid the writing error from P to AP due to the back-hopping of FL_2.

4. Conclusion

We demonstrated a successful design approach to ultra-scaled STT-MRAM consisting of several elongated pieces of ferromagnets separated by multiple tunnel barriers. The interface-induced anisotropy and the position-dependence of the transverse spin dephasing length are taken into account and the influence of these effects on the magnetization dynamics as well as their role in the proper modeling of the switching behavior in ultra-scaled MRAM cells is investigated. Furthermore, we analyzed how the switching behavior depends on the length of the composite free layer sections, and failure mechanism due to the back-hopping of a FL section is revealed. The predictions from our simulation results agree well with recent experimental demonstrations of switching of ultra-scaled MRAM cells.

Declaration of competing interest

The authors declare that they have no known competing financial interests or personal relationships that could have appeared to influence the work reported in this paper.

Data availability

Data will be made available on request.

Acknowledgments

The financial support by the Austrian Federal Ministry for Digital and Economic Affairs, the National Foundation for Research, Technology and Development, Austria, and the Christian Doppler Research Association, Austria is gratefully acknowledged. The authors acknowledge TU Wien Bibliothek, Austria for financial support through its Open Access Funding Program.

References

[1] Ito T, Saito T, Taito Y, Sonoda K, Watanabe G, et al. A 20Mb embedded STT-MRAM array achieving 72% write energy reduction with self-termination write schemes in 16nm FinFET logic process. In: 2021 IEEE international electron devices meeting (IEDM). 2021, p. 2.2.1–4. http://dx.doi.org/10.1109/IEDM19574.2021.9720523.

[2] Chiu Y-C, Yang C-S, Teng S-H, Huang H-Y, Chang F-C, et al. A 22nm 4Mb STT-MRAM data-encrypted near-memory computation macro with a 192GB/s read-and-decryption bandwidth and 25.1-55.1TOPS/W 8b MAC for AI operations. In: 2022 IEEE international solid- state circuits conference (ISSCC), vol. 65. 2022, p. 178–80. http://dx.doi.org/10.1109/ISSCC42614.2022.9731621.

[3] Sun JJ, DeHerrera M, Hughes B, Ikegawa S, Lee HK, et al. Commercialization of 1Gb standalone spin-transfer torque MRAM. In: 2021 IEEE international memory workshop (IMW). 2021, p. 1–4. http://dx.doi.org/10.1109/IMW51353.2021.9439616.

[4] Barla P, Joshi VK, Bhat S. Spintronic devices: a promising alternative to CMOS devices. J Comput Electr 2021;20:805–37. http://dx.doi.org/10.1007/s10825-020-01648-6.

[5] Ikegawa S, Mancoff FB, Janesky J, Aggarwal S. Magnetoresistive random access memory: Present and future. IEEE Trans Electron Devices 2020;67:1407–19. http://dx.doi.org/10.1109/TED.2020.2965403.

[6] Peng S, Zhu D, Zhou J, Zhang B, Cao A, et al. Modulation of heavy metal/ferromagnetic metal interface for high-performance spintronic devices. Adv Electr Mater 2019;5:1900134. http://dx.doi.org/10.1002/aelm.201900134.

[7] Ikeda S, Miura K, Yamamoto H, Mizunuma K, Gan HD, et al. A perpendicular-anisotropy CoFeB–MgO magnetic tunnel junction. Nature Mater 2010;9:721–4. http://dx.doi.org/10.1038/nmat2804.

[8] Shi K, Cai W, Jiang S, Zhu D, Cao K, et al. Observation of magnetic droplets in magnetic tunnel junctions. Sci China Phys Mech Astron 2022;65.

[9] Cai W, Wang M, Cao K, Yang H, Peng S, othersg. Stateful implication logic based on perpendicular magnetic tunnel junctions. Sci China Inf Sci 2022;65. http://dx.doi.org/10.1007/s11432-020-3189-x.

[10] Su J, Li G, Bai H, Zhu ZZ, Zhang Y, et al. Large perpendicular magnetic anisotropy and tunneling magnetoresistance in thermally stable Mo/FeNiB/MgO magnetic tunnel junctions. J Phys D: Appl Phys 2020;53:125003. http://dx.doi.org/10.1088/1361-6463/ab6626.

[11] Jinnai B, Igarashi J, Watanabe K, Funatsu T, Sato H, et al. High-performance shape-anisotropy magnetic tunnel junctions down to 2.3 nm. In: 2020 IEEE international electron devices meeting (IEDM). 2020, p. 24.6.1–4. http://dx.doi.org/10.1109/IEDM13553.2020.9371972.

[12] Khanal P, Zhou B, Andrade M, Dang Y, Davydov A, et al. Perpendicular magnetic tunnel junctions with multi-interface free layer. Appl Phys Lett 2021;119:242404. http://dx.doi.org/10.1063/5.0066782.

[13] Camsari KY, Ganguly S, Datta D, Datta S. Physics-based factorization of Magnetic Tunnel Junctions for modeling and circuit simulation. In: 2014 IEEE international electron devices meeting. 2014, p. 35.6.1–4. http://dx.doi.org/10.1109/IEDM.2014.7047177.

[14] Haney PM, Lee H-W, Lee K-J, Manchon A, Stiles MD. Current induced torques and interfacial spin-orbit coupling: Semiclassical modeling. Phys Rev B 2013;87:174411. http://dx.doi.org/10.1103/PhysRevB.87.174411.

[15] Slonczewski JC. Currents, torques, and polarization factors in magnetic tunnel junctions. Phys Rev B 2005;71:024411. http://dx.doi.org/10.1103/PhysRevB.71.024411.

[16] Brataas A, Bauer GE, Kelly PJ. Non-collinear magnetoelectronics. Phys Rep 2006;427:157–255. http://dx.doi.org/10.1016/j.physrep.2006.01.001.

[17] Anderson R, Andrej J, Barker A, Bramwell J, Camier J-S, et al. MFEM: A modular finite element methods library. Comput Math Appl 2021;81:42–74. http://dx.doi.org/10.1016/j.camwa.2020.06.009.

[18] Ender J, Mohamedou M, Fiorentini S, Orio R, Selberherr S, Goes W, Sverdlov V. Efficient demagnetizing field calculation for disconnected complex geometries in STT-MRAM cells. In: 2020 International conference on simulation of semiconductor processes and devices (SISPAD). 2020, p. 213–6. http://dx.doi.org/10.23919/SISPAD49475.2020.9241662.

[19] Abert C, Ruggeri M, Bruckner F, Vogler C, Manchon A, et al. A self-consistent spin-diffusion model for micromagnetics. Sci Rep 2016;6. http://dx.doi.org/10.1038/s41598-016-0019-y.

[20] Abert C, Ruggeri M, Bruckner F, Vogler C, Hrkac G, et al. A three-dimensional spin-diffusion model for micromagnetics. Sci Rep 2015;5. http://dx.doi.org/10.1038/srep14855.

[21] Lepadatu S. Unified treatment of spin torques using a coupled magnetisation dynamics and three-dimensional spin current solver. Sci Rep 2017;7. http://dx.doi.org/10.1038/s41598-017-13181-x.

[22] Petitjean C, Luc D, Waintal X. Unified drift-diffusion theory for transverse spin currents in spin valves, domain walls, and other textured magnets. Phys Rev Lett 2012;109:117204. http://dx.doi.org/10.1103/PhysRevLett.109.117204.

[23] Fiorentini S, Ender J, Selberherr S, de Orio R, Goes W, Sverdlov V. Coupled spin and charge drift-diffusion approach applied to magnetic tunnel junctions. Solid-State Electron 2021;186:108103. http://dx.doi.org/10.1016/j.sse.2021.108103.

[24] Nishioka K, Honjo H, Ikeda S, Watanabe T, Miura S, et al. Novel quad-interface MTJ technology and its first demonstration with high thermal stability factor and switching efficiency for STT-MRAM beyond 2X nm. IEEE Trans Electron Devices 2020;67(3):995–1000. http://dx.doi.org/10.1109/TED.2020.2966731.

Mario Bendra was born in Steyr, Austria, in 1993. He received his Bachelor degree in Mechanical Engineering from the University of Applied Sciences Upper Austria in 2017. After an exchange semester at the University of the Sunshine Coast, Australia, in 2018, he received the degree of Diplomingenieur in Mechanical Engineering from the University of Applied Sciences Upper Austria in 2019. Mario joined the Christian Doppler Laboratory on Nonvolatile Magnetoresistive Memory and Logic in October 2020, where he is working towards his doctoral degree. His primary focus is developing and implementing advanced computational approaches to simulate and optimize spin-transfer torque in magnetoresistive memories.